

Seasonal sea-ice in the Arctic's last ice area during the Early Holocene

Henrieka Detlef^{1,2✉}, Matt O'Regan³, Christian Stranne³, Mads Mørk Jensen⁴, Marianne Glasius^{2,4}, Thomas M. Cronin⁵, Martin Jakobsson³ & Christof Pearce^{1,2✉}

According to climate models, the Lincoln Sea, bordering northern Greenland and Canada, will be the final stronghold of perennial Arctic sea-ice in a warming climate. However, recent observations of prolonged periods of open water raise concerns regarding its long-term stability. Modelling studies suggest a transition from perennial to seasonal sea-ice during the Early Holocene, a period of elevated global temperatures around 10,000 years ago. Here we show marine proxy evidence for the disappearance of perennial sea-ice in the southern Lincoln Sea during the Early Holocene, which suggests a widespread transition to seasonal sea-ice in the Arctic Ocean. Seasonal sea-ice conditions were tightly coupled to regional atmospheric temperatures. In light of anthropogenic warming and Arctic amplification our results suggest an imminent transition to seasonal sea-ice in the southern Lincoln Sea, even if the global temperature rise is kept below a threshold of 2 °C compared to pre-industrial (1850–1900).

¹Department of Geoscience, Aarhus University, Aarhus, Denmark. ²Arctic Research Centre, Aarhus University, Aarhus, Denmark. ³Department of Geological Sciences, Stockholm University, Stockholm, Sweden. ⁴Department of Chemistry, Aarhus University, Aarhus, Denmark. ⁵U.S. Geological Survey, Florence Bascom Geoscience Center, National Center, 12201 Sunrise Valley Drive, Reston, VA, USA. ✉email: henrieka.detlef@geo.au.dk; christof.pearce@geo.au.dk

The observed demise of Arctic sea-ice in recent decades¹ has had major impacts on the climate, the ecosystem, the livelihood and cultural heritage of Indigenous peoples, and global geopolitical interests^{2–4}. As anthropogenic warming continues, climate models suggest that Arctic multi-year ice (MYI) will survive the longest along the northern coastline of the Canadian Arctic Archipelago and Greenland^{5–11}. Today this region, also known as the last ice area (hereafter referred to as LIA), hosts the thickest and oldest sea-ice in the Arctic Ocean^{12,13}. This is due to cold temperatures and the main Arctic Ocean surface circulation, dominated by the Beaufort Gyre and the Transpolar Drift, transporting sea-ice toward the LIA^{13,14}. As a result, the LIA is perennially covered by a mixture of locally formed and transported first year ice (FYI) and MYI with ages greater than 5 years¹². The dominant source regions of MYI in the LIA today are traced to the Eurasian and Amerasian shelves¹⁵.

Within the LIA, between northeastern Ellesmere Island and Greenland, lies the Lincoln Sea (Fig. 1), one of the least studied marginal seas of the Arctic Ocean¹⁶. In recent years, more and more evidence for a changing sea-ice cover in the Lincoln Sea region has emerged, questioning its long-term stability under a continued anthropogenic warming. Prolonged periods of open water are reported from east of the Lincoln Sea and north of Ellesmere Island^{17,18} and increased ice motion¹⁹ and loss of the oldest MYI¹² are associated with recurrent failure of the Nares Strait ice arches^{20–22}. These phenomena are likely related to both physical and thermodynamic processes, where anomalous atmospheric circulation and break-up and export of sea-ice by winds^{17,21} causes an increase in the open water and thin ice area fractions enhancing ice melt¹⁷.

As climate model projections for the 21st century agree that the LIA will host the last remaining summer sea-ice in the

Arctic^{6–11,23,24}, by first principle, a transition to seasonal sea-ice in the LIA would be indicative of a sea-ice regime shift in the entire Arctic Ocean. Applying this principle to previous warm periods in the geological past can thus elucidate the resilience of the Arctic Ocean sea-ice cover to climate change.

In 2019, the Swedish icebreaker *Oden* set out on the *Ryder 2019* Expedition to map and retrieve marine sediment cores from the uncharted Sherard Osborn Fjord and southeastern Lincoln Sea (Fig. 1). Here we examine Holocene sea-ice dynamics based on two gravity cores (Ryder19-12-GC1, Ryder19-14-GC1; hereafter referred to as 12-GC and 14-GC) and 15 multi-core surface samples from the southern Lincoln Sea (Fig. 1). The age models are based on lithological investigations and radiocarbon dating, indicating that the entire Holocene period was recovered. The Early Holocene, characterized by a peak in boreal summer insolation²⁵, represents the most recent period in geological history when temperatures were similar to or possibly exceeded modern observations²⁶. Although the causes of modern warming differ, similar climate boundary conditions suggest that the Early Holocene may be a suitable analogue to understand the configuration of the Arctic climate system in a warmer future. Using a coupled atmosphere-sea-ice-ocean column model, Stranne et al.²⁷ suggest the possibility of an Arctic Ocean-wide transition to a seasonal sea-ice regime during the Early Holocene, supported by data from the Eurasian and Amerasian Arctic shelves^{28–30}, the Beaufort Sea³¹, the Greenland Sea^{32–36}, and the central Arctic Ocean^{37,38}. Within the LIA, reduced MYI during the Early Holocene is supported by coastal records of beach ridges and driftwood from northern Greenland and Ellesmere Island^{39,40}. However, no data exist from the marine realm, critical to assess whether the change to a seasonal sea-ice regime in the Early Holocene impacted the LIA and by extension the entire Arctic Ocean.

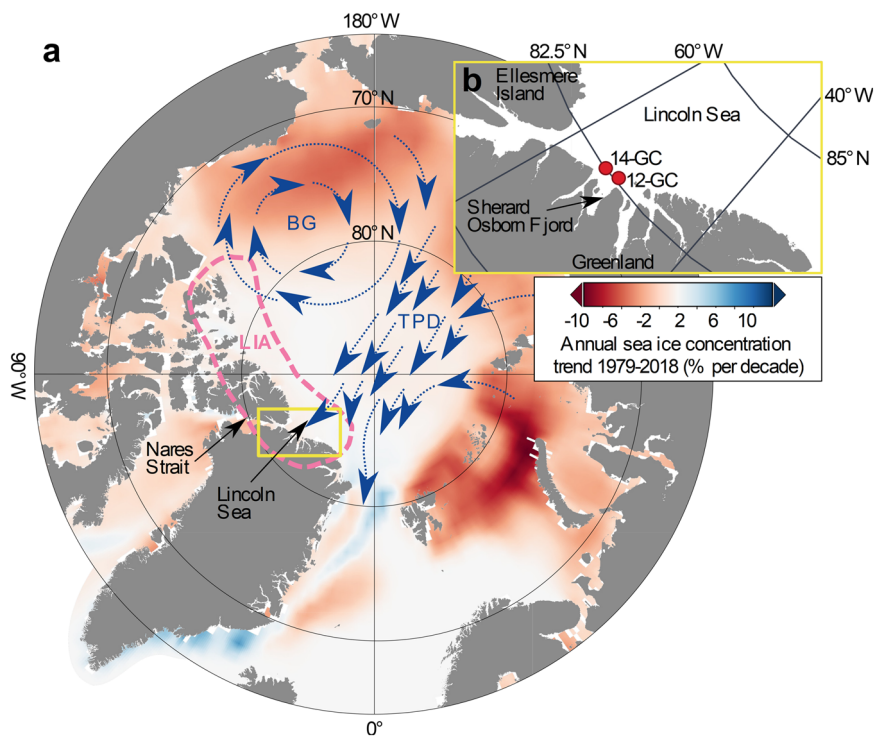


Fig. 1 Sea-ice concentration trend in the Arctic Ocean and core locations in the Lincoln Sea. **a** Map of the Arctic Ocean including the annual sea-ice concentration trend from 1979 to 2018⁹⁴ (and references therein) and the major surface circulation features, the Transpolar Drift (TPD) and Beaufort Gyre (BG) (dashed blue arrows). The dashed pink line outlines the region of the last ice area (LIA) that lies within the Arctic Ocean proper. The trend in sea-ice concentration is shown as % per decade, i.e. the decrease/increase of sea-ice concentration per 10-years for the period from 1979 to 2018. **b** Close-up of the Lincoln Sea (yellow rectangle in **a**) including locations of core sites Ryder19-12-GC1 (12-GC) and Ryder19-14-GC1 (14-GC).

Results and Discussion

Holocene sea-ice dynamics in the Lincoln Sea. Our reconstruction of Holocene sea-ice dynamics in the Lincoln Sea is based on the analysis of sympagic (IP₂₅, HBI II) and pelagic (brassicasterol) biomarkers⁴¹ and the amount of total organic carbon (TOC). Changes in the relative concentration of the individual biomarker groups are indicative of changes in ice algal versus open water habitats through time⁴¹, while TOC provides more general information on the accumulation of organic matter in the sediments. In surface sediments underlying the pack ice area of the central Arctic, biomarker concentrations and TOC are low/absent⁴² as primary productivity is restricted by the availability of nutrients and photosynthetically active radiation⁴³. In general, sympagic biomarker concentrations are highest in surface sediments in regions of seasonal sea-ice and along the ice edge, while they are absent in ice-free regions⁴². The concentration of brassicasterol is elevated in the seasonal ice zone, as well as in ice-free regions in line with a broad pelagic source⁴².

Accordingly, elevated concentrations of both sympagic and pelagic biomarkers in 12-GC and 14-GC between approximately 11.3 ± 0.6 cal ka BP and 9.7 ± 0.6 cal ka BP indicate a period of seasonal sea-ice during the Early Holocene (Fig. 2, Supplementary Fig. 1). The close correlation of IP₂₅ and brassicasterol throughout this interval suggests that the presence/absence of sea-ice governed both sympagic and pelagic productivity, as is expected in the marginal ice zone or environments with relatively short-lived ice-free periods during summer^{42,44,45}. This is

supported by the P_BIP₂₅ index (Fig. 2) with a mean value of 0.5 ($n = 33$), considered to reflect a seasonally ice-free/marginal sea-ice environment. After ~9.7 ± 0.6 cal ka BP, a drop in all biomarker concentrations (Fig. 2) and a decrease in the amount of TOC (Fig. 2) suggests the (re-)establishment of a perennial sea-ice cover in the southern Lincoln Sea. Throughout the mid-to-late Holocene, biomarker concentrations remain low, while TOC increases again to intermediate levels after ca. 8 cal ka BP (Fig. 2). This is in line with a more persistent sea-ice cover compared to the Early Holocene. However, short-term (centennial) variability cannot be resolved throughout this interval due to the relatively lower sedimentation rates (1–40 cm/kyr) compared to the Early Holocene (50–125 cm/kyr). In the topmost samples of both cores (5.5 cm/~2 cal ka BP and 1 cm/~1 cal ka BP in 12-GC and 14-GC, respectively) the concentrations of sympagic and to a lesser extent pelagic biomarkers increase once again (Fig. 2). Due to the low sedimentation rates and bioturbation, these values are likely influenced by modern sea-ice variability and are consistent with the relatively high biomarker concentrations in the 15 surface samples from the region (Supplementary Fig. 2) (Supplementary discussion 2.2). The surface samples yield P_BIP₂₅ values of 0.6–0.8 (Supplementary discussion 2.2) (Fig. 2, Supplementary Fig. 2), which are slightly lower than during the mid-to-late Holocene and indicative of seasonal to perennial sea-ice. The decrease in P_BIP₂₅ likely reflects recently observed reductions in the LIA sea-ice concentration^{17,18,20,46} (Figs. 2, 3) and the beginning of the transition towards a more variable/seasonal sea-ice regime in the southern Lincoln Sea.

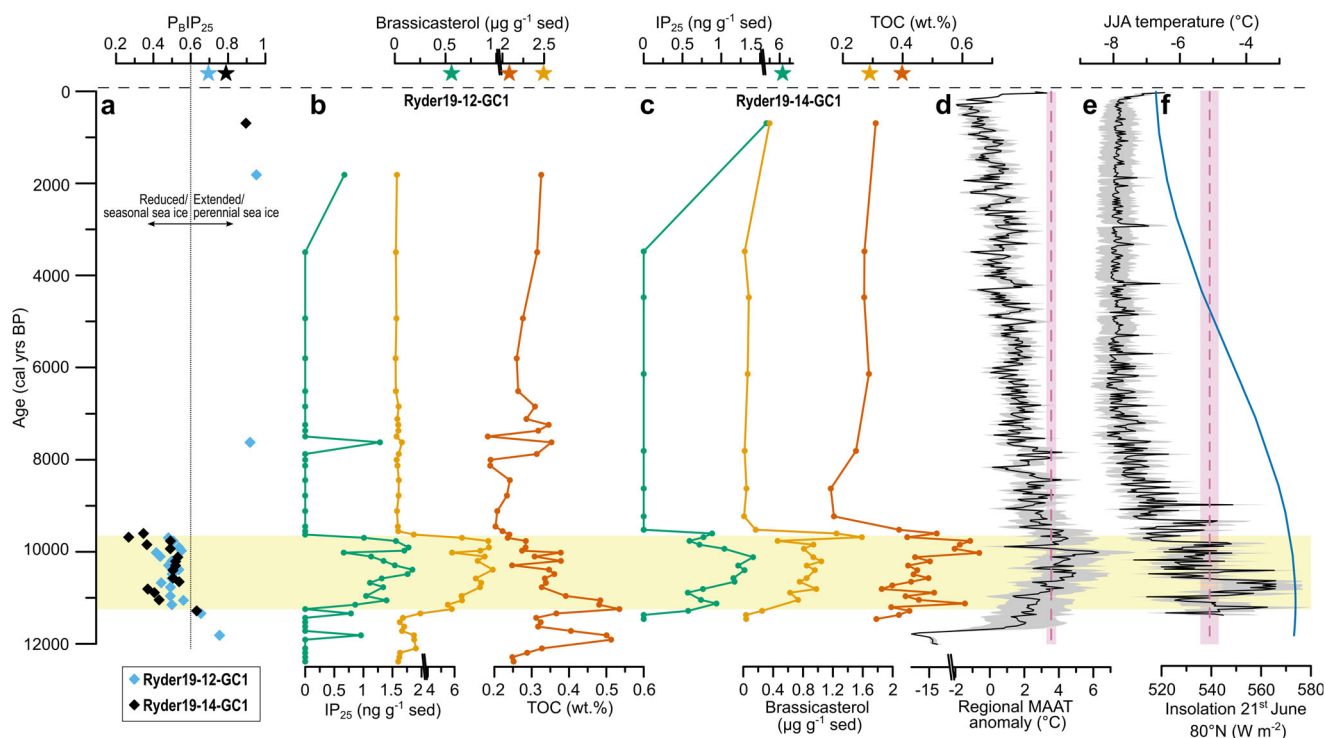


Fig. 2 Sea-ice biomarkers and TOC from two sites in the Lincoln Sea alongside regional atmospheric temperatures across the Holocene. **a** P_BIP₂₅ in Ryder19-12-GC1 (light blue diamonds) and Ryder19-14-GC1 (black diamonds). **b** IP₂₅ (green), brassicasterol (yellow), and TOC (orange) in Ryder19-12-GC1. **c** IP₂₅ (green), brassicasterol (yellow), and TOC (orange) in Ryder19-14-GC1. **d** Mean annual air temperature anomaly (MAAT) at Agassiz ice cap compared to pre-industrial (PI; Supplementary Methods 1.2) (black) including the 2 σ uncertainty envelope (grey)⁶¹. MAAT was reconstructed based on the oxygen isotopic signature ($\delta^{18}\text{O}$) in the ice⁶¹. Additionally the mean of the Early Holocene time period with evidence for seasonal sea-ice (dashed pink) with the corresponding 95% confidence interval (light pink) is shown. **e** Reconstructed June-August temperatures at Agassiz ice cap (black) based on the melt layer record including the 2 σ uncertainty envelope (grey)⁶¹ and the mean of the Early Holocene time period with evidence for seasonal sea-ice (dashed pink) with the corresponding 95% confidence interval (light pink). **f** 21st of June insolation at 80°N⁹⁵ (blue). The stars above the horizontal dashed line show P_BIP₂₅ (light blue, black), IP₂₅ (green), brassicasterol (yellow), and TOC (orange) in the surface samples of Ryder19-12-MC1-8 and Ryder19-13-MC1-5 (Fig. 4). The horizontal light yellow bar marks the Early Holocene interval characterized by seasonal sea-ice in the southern Lincoln Sea.

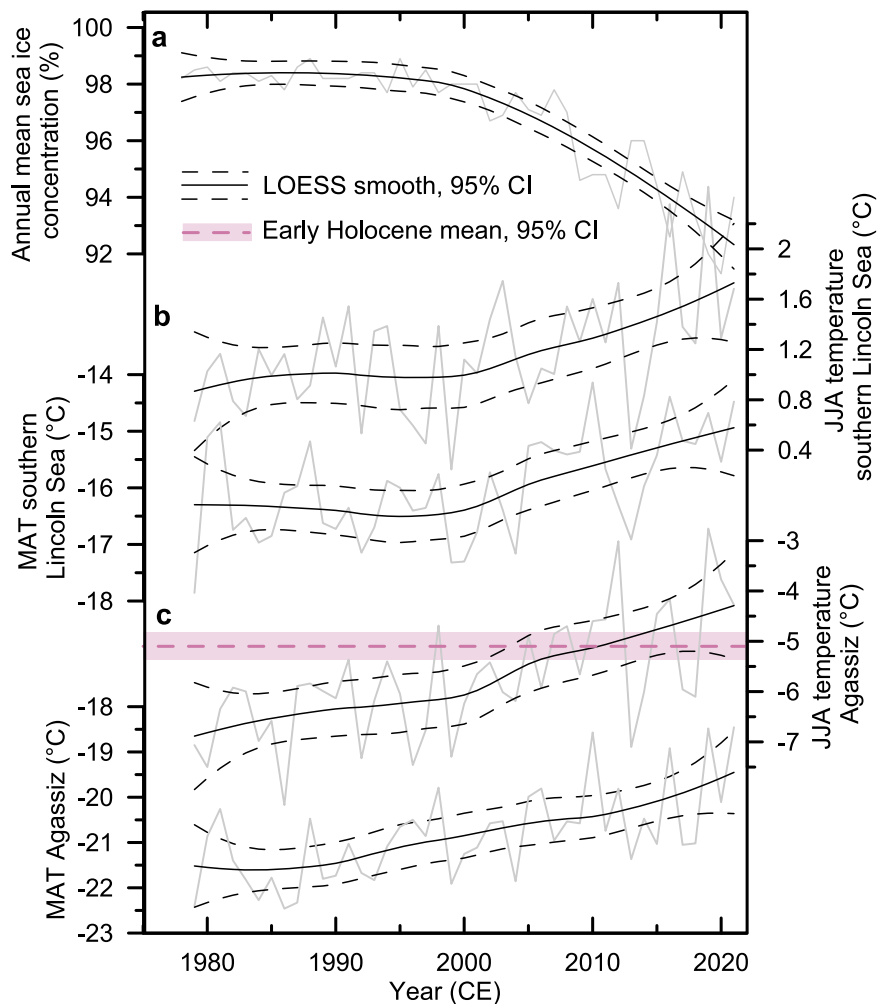


Fig. 3 Modern sea-ice, mean annual and summer temperatures in the southern Lincoln Sea region. **a** Annual mean sea-ice concentration in the southern Lincoln Sea (grey) including the LOESS (locally weighted scatterplot smoothing) smooth (black) and the 95% confidence interval (dashed black) from the Pan-Arctic Ice Ocean Modeling and Assimilation System (PIOMAS), 1978–2021⁶⁵. **b** JJA and mean annual temperatures at a location proximal to 12-GC and 14-GC (82.5 °N, 55 °W, 0 m MSL) from the ERA5 reanalysis (2 m atmospheric temperatures)⁶⁴ (light grey) and the respective LOESS smooth (black) including the 95% confidence interval (dashed black), 1979–2021. **c** JJA and mean annual temperatures proximal to the Agassiz ice cores (80.75 °N, 73 °W, 1740 m MSL) from the ERA5 reanalysis (2 m atmospheric temperatures)⁶⁴ (light grey) and the respective LOESS smooth (black) including the 95% confidence interval (dashed black), 1979–2021. The average of JJA temperatures for the Early Holocene interval characterized by seasonal sea-ice (dashed pink) and the 95% confidence interval (light pink) are included in the plot of JJA temperatures at the Agassiz ice cap.

Micropaleontological data from 12-GC and 14-GC support a shift from reduced sea-ice during the Early Holocene to a more persistent ice cover during the mid-to-late Holocene⁴⁷ (Supplementary Fig. 3, Supplementary Fig. 4). Between ca. 11.3 ± 0.6 cal ka BP and 9.7 ± 0.6 cal ka BP the benthic foraminiferal species *Cassidulina neoteretis*, typically associated with bottom waters of Atlantic origin⁴⁸, dominates the assemblage in both cores (Supplementary Fig. 3, Supplementary Fig. 4). While *C. neoteretis* also dominates during the mid-to-late Holocene, other species, such as *Oridorsalis umbonatus*, become more important (Supplementary Fig. 3, Supplementary Fig. 4)⁴⁷. In the Arctic Ocean, *O. umbonatus* is characteristic of areas with a dense sea-ice cover and low export of organic carbon to the seafloor⁴⁹. An increase in *O. umbonatus* in the southern Lincoln Sea around 9.7 ± 0.6 cal ka BP (especially pronounced in 14-GC, Supplementary Fig. 4) thus supports the re-establishment of a perennial ice cover around this time. Similar to the benthic foraminifera, the ostracod assemblage during the mid-to-late Holocene suggests the presence of a persistent ice cover (Supplementary Fig. 3, Supplementary Fig. 4)⁴⁷. Although *Polycope* spp. is

typically described as a genus associated with seasonal/marginal sea-ice environments^{50,51}, it also occurs in surface sediments of the central Arctic Ocean under perennial sea-ice^{52,53} and may be associated with the upper Arctic Ocean Deep Water and/or lower Arctic Intermediate Water affected by waters of Atlantic origin^{53,54}. In the southern Lincoln Sea, *C. neoteretis* bears witness to bottom waters of Atlantic origin throughout the entire Holocene, which might explain the presence of *Polycope* spp. during the mid-to-late Holocene (Supplementary Fig. 3, Supplementary Fig. 4). At the same time, the ostracod species *Acetabulastoma arcticum* is present in all samples younger than ~9.2 cal ka BP in 14-GC (Supplementary Fig. 4) and in one sample in 12-GC (ca. 6.2 cal ka BP)⁴⁷. *A. arcticum* lives parasitically on the under-ice amphipod *Gammarus*, found exclusively in the brackish surface layer underneath pack ice⁵². Thus, it can be used as an indicator of a perennial sea-ice cover such as in the central Arctic Ocean today³⁸ and does not occur on continental shelves characterized by seasonally ice-free conditions⁵². The exclusive (apart from one sample in 14-GC) presence of *A. arcticum* in samples younger than ca. 9.2 cal ka BP

therefore supports the re-establishment of a perennial ice cover in the southern Lincoln Sea during the mid-to-late Holocene.

Other Arctic biomarker records that cover the Early Holocene are from the outer and inner northeast Greenland Shelf^{35,36}, the eastern Fram Strait/Yermak Plateau^{33,34}, the Barents Sea north of Svalbard³², the inner and outer Laptev Sea^{29,30,55}, and the Beaufort Sea³¹ (Supplementary Fig. 5). All available records show a reduction in the sea-ice extent during the Early Holocene, with most records suggesting this decrease occurred earlier than in the Lincoln Sea (Supplementary Fig. 5). In the Beaufort Sea, reduced sea-ice occurs from the onset of the record at 14 cal ka BP³¹. In the inner and outer Laptev Sea, biomarker records suggest a reduction in sea-ice extent following the Younger Dryas around 11.8 cal ka BP^{29,30,55} and in the northernmost Barents Sea sea-ice retreats around 11.6 cal ka BP³² (Supplementary Fig. 5). Three records in proximity to the southern Lincoln Sea are from areas of perennial sea-ice cover in the northernmost Barents Sea³² (JR142-11GC, HH-15-06GC) and on the inner NE Greenland shelf (PS100/270-1), covered by the landfast Norske Øer Ice Barrier³⁶. They show similar temporal characteristics to the southern Lincoln Sea, with increased biomarker concentrations during the Early Holocene and a drop in concentrations/fluxes at 9.1 cal ka BP and 9.6 cal ka BP in the northernmost Barents Sea and on the NE Greenland shelf, respectively^{32,36} (Supplementary Fig. 5). The re-establishment of a perennial ice cover in the Atlantic sector of the Arctic Ocean/northernmost Greenland Sea thus closely follows that of the southern Lincoln Sea around 9.7 ± 0.6 cal ka BP (Fig. 2, Supplementary Fig. 5). An earlier sea-ice retreat, as well as a later re-establishment of a perennial ice cover in regions outside the LIA agree with the LIA being the last (first) region of MYI in a warming (cooling) climate and suggest that the transition to seasonal sea-ice in the LIA during the early Holocene was equivalent to a regime shift in large parts of Arctic Ocean.

On the other hand, some contrasting sedimentary and micropaleontological evidence exists from the central Arctic Ocean. While de Vernal et al.⁵⁶ suggest that perennial sea-ice persisted over the western and central Lomonosov Ridge during the Early Holocene, Hanslik et al.³⁷ and Cronin et al.³⁸ suggest an interval of reduced sea-ice in the central Arctic Ocean from approximately 11.6–10 ka³⁷. Due to low sedimentation rates in the central Arctic Ocean, however, the Early Holocene is typically only represented by 2–3 datapoints^{37,38,56}, which might not resolve the sea-ice variability. If sea-ice persisted in the central Arctic Ocean during the Early Holocene, seasonal sea-ice in the southern Lincoln Sea was likely restricted to the near-coastal areas, associated with a thinner more mobile sea-ice cover and the breakdown of the landfast sea-ice cover. In this scenario, a thin ice pack may have survived in the central Lincoln Sea and parts of the central Arctic Ocean.

Mechanisms destabilizing the sea-ice cover in the Lincoln Sea across the Holocene. Following the last deglaciation, the Early Holocene was a time of rapid climate and environmental change. Rising summer insolation in the northern hemisphere resulted in Early Holocene warmth in the Arctic and subarctic realm⁵⁷. Atmospheric warming was most pronounced during summer, with large parts of Greenland experiencing summer temperatures warmer than those of the mid-twentieth century by about 10 ka⁵⁸. A review of available ice core records suggests that the north-western and central Greenland Ice Sheet (GrIS) may have experienced summer temperatures 3–5 °C warmer compared to the mid-twentieth century, while the southern GrIS may only have experienced warming of up to 1–2 °C⁵⁸. In addition to the spatial heterogeneity of Early Holocene warmth, the timing varies

depending on latitude and in continental versus marine records^{59,60}. In general, a Holocene Thermal Maximum (HTM) occurs earlier in high latitude marine records (11–7 ka) than at lower latitudes and in continental records (8–4 ka)⁶⁰. Ice cores from the Agassiz ice cap on Ellesmere Island provide a record of Holocene mean annual air temperature anomalies (MAAT) (compared to PI; Supplementary Methods 1.2) and June–August temperatures (T_{JJA}) in close proximity to the southern Lincoln Sea⁶¹. These demonstrate a regional HTM between 11 ka and 8 ka, during which temperatures regularly exceeded present-day values⁶¹ (Fig. 2). Peak Holocene temperatures at Agassiz ice cap thus occur earlier compared to ice core records from Greenland⁵⁸, in line with an early HTM at higher latitudes⁶⁰. Maximum Early Holocene temperatures at Agassiz ice cap are associated with the largest accumulation rate of pollen grains⁶¹, indicating a more productive terrestrial ecosystem in close proximity to the ice cap.

The regional HTM as recorded at Agassiz ice cap (11–8 ka) is concomitant with the evidence of seasonal sea-ice in the southern Lincoln Sea between approximately 11.3 ± 0.6 cal ka BP and 9.7 ± 0.6 cal ka BP (Fig. 2), suggesting that atmospheric temperatures likely played an important role for Early Holocene sea-ice conditions. This is supported by climate model simulations, which show that warming from increased radiative forcing may have been enough to shift the Arctic Ocean from a perennial to a predominantly seasonal sea-ice regime during the Early Holocene²⁷. Other models, however, only show a reduction in sea-ice concentration in the Arctic marginal seas, while sea-ice thickness decreases everywhere in the Arctic when the Early Holocene radiative forcing is applied⁶². Thus, in addition to atmospheric warming other factors may have contributed to decrease the Early Holocene sea-ice extent in the southern Lincoln Sea. Biomarker-based sea-ice reconstructions from the Amerasian and Eurasian Arctic shelves indicate a reduction in sea-ice extent already between 14 ka and 11.8 ka^{28–30,63}, earlier than in the Lincoln Sea (Fig. 2, Supplementary Fig. 5). Today, these regions comprise the dominant source areas of MYI to the Lincoln Sea¹⁵. Thus, an early decline in sea-ice extent likely caused a reduction in the net transport of sea-ice towards the LIA from as early as 14 ka. Other mechanisms, which might have contributed to a reduction in the sea-ice extent in the Lincoln Sea, include increased freshwater discharge from the GrIS and enhanced export of sea-ice through Fram Strait (Supplementary discussion 2.1).

Based on the LIA dataset and in combination with previously published records of Holocene sea-ice variability from across the Arctic and subarctic realm^{28–30,32–38,56} we thus argue that the Arctic Ocean likely transitioned to a predominantly seasonal sea-ice regime during the Early Holocene, while some areas in the central Lincoln Sea and adjacent central Arctic Ocean may have retained a thin ice pack. The early decline in sea-ice extent in the LIA MYI source regions and the associated reduction in net sea-ice transport towards the Lincoln Sea likely resulted in a thinner, younger, and more mobile ice cover, which made the LIA more vulnerable to atmospheric and oceanic forcing during the regional HTM resulting in the observed seasonal sea-ice signal.

This is consistent with modelling experiments of the MYI source regions to the LIA under future warming scenarios¹⁵. In a high warming scenario, corresponding to the representative concentration pathway 8.5, net sea-ice transport to the LIA ceases and the LIA transitions from predominantly MYI to FYI with ice free summers¹⁵. In a low warming scenario, consistent with a global warming threshold of 2 °C compared to the PI, on the other hand, the central Arctic Ocean becomes the dominant source region together with increased in situ formation of sea-ice¹⁵. Both scenarios are associated with a more mobile and thinner ice pack in the LIA compared to the historical record¹⁵.

Implications for future sea-ice dynamics in the Lincoln Sea. In the following section, we are discussing the implications of the early Holocene sea-ice conditions in the Lincoln Sea for the future stability of sea-ice in the LIA. Given the correlation of sea-ice and atmospheric temperatures during the early Holocene, we are focusing on atmospheric temperatures as the main driver of sea-ice change, not considering additional drivers such as changes in the Arctic Ocean surface circulation, effects of freshwater addition to the Arctic Ocean, and local sea-ice dynamics, including the formation of ice arches in Nares Strait.

The interval of seasonal sea-ice in the southern Lincoln Sea from $\sim 11.3 \pm 0.6$ to 9.7 ± 0.6 cal ka BP was characterized by mean $T_{JJA} -5.1 \pm 1.1$ °C and MAAT (compared to PI; Supplementary Methods 1.2) of 3.6 ± 1.1 °C as reconstructed from the Agassiz ice cores⁶¹ (Fig. 2). Modern (2009 CE) MAAT at Agassiz ice cap are ~ 3.1 °C (compared to PI)⁶¹, while the reconstructed T_{JJA} time series stops at 1934 CE. Thus, to further compare Early Holocene and modern temperature and sea-ice dynamics, the mean annual temperature (MAT) and T_{JJA} from 1979–2021 were extracted from the ERA5 reanalysis⁶⁴ (Fig. 3) at two locations corresponding to Agassiz ice cap (80.75 °N, 73 °W, 1740 m MSL) and sea-level in close proximity to the coring sites (82.5 °N, 55 °W, 0 m MSL) (Fig. 4). The annual mean sea-ice concentration (1978–2021) was extracted from the Pan-Arctic Ice Ocean Modeling and Assimilation System (PIOMAS)⁶⁵ (Fig. 3). Sea-ice concentration data were averaged over an area corresponding to the southern Lincoln Sea (Fig. 4).

MAT and T_{JJA} at Agassiz ice cap and in the southern Lincoln Sea are significantly correlated (MAT Agassiz \sim Lincoln Sea: $R^2 = 0.77$, $P < 0.001$; T_{JJA} Agassiz \sim Lincoln Sea: $R^2 = 0.70$, $P < 0.001$) with a mean difference of 4.9 ± 0.7 °C and 6.9 ± 0.9 °C for MAT and T_{JJA} , respectively. This suggests that both the MAT and summer temperature at Agassiz ice cap are representative of those in the southern Lincoln Sea. Between 1979 and 2021, MAT/

T_{JJA} show a significant warming trend of $0.5/0.6$ °C ($P < 0.001$) per decade at Agassiz ice cap and $0.4/0.2$ °C ($P < 0.001$) per decade in the Lincoln Sea (Fig. 3). Throughout the record, T_{JJA} at Agassiz ice cap exceeded the Early Holocene mean of -5.1 ± 1.1 °C in 12 out of 43 years, with six occasions during the last decade (Fig. 3). This indicates that both the MAAT (3.1 °C as reconstructed from Agassiz ice core⁶¹) and T_{JJA} (from ERA5) at Agassiz ice cap are approaching levels last seen during the Early Holocene.

Simultaneously, the mean annual sea-ice concentration in the southern Lincoln Sea⁶⁵ decreased with -1.4 % per decade ($P < 0.001$) from 1979–2021 and with -2.7 % per decade ($P < 0.001$) from 2000 onwards (Fig. 3). This is consistent with the observed signs of a changing sea-ice cover in the wider LIA region during recent years^{17,18,21,46} and the decrease in P_{BIP25} in surface sediments compared to the mid-to-late Holocene (Fig. 2, Supplementary Fig. 2) (Supplementary discussion 2.2). Lincoln Sea MAT and T_{JJA} and the annual mean sea-ice concentration show a significant negative correlation between 1979 and 2021 (MAT \sim sea-ice: $R^2 = -0.56$, $P < 0.001$; $T_{JJA} \sim$ sea-ice: $R^2 = -0.62$, $P < 0.001$) (Supplementary Fig. 6), supporting a prominent role of atmospheric temperatures (both MAT and T_{JJA}) for sea-ice dynamics in the southern Lincoln Sea.

At the 21st conference of the United Nations Framework Convention on Climate Change (COP21), 196 parties adopted ‘The Paris Agreement’ to limit mean global warming to 1.5 – 2 °C (compared to PI levels; 1850–1900). As a result of Arctic amplification, a global mean warming of 2 °C compared to PI would result in a mean annual air temperature increase of 3 – 5 °C (compared to the PI) in the Arctic⁶⁶. Different estimates exist for Arctic warming during the Early Holocene. Based on 16 terrestrial sites from the western Arctic, Kaufman et al.⁶⁷ suggest that summer temperatures warmed on average 1.6 ± 0.8 °C (compared to the 20th century average). Climate model

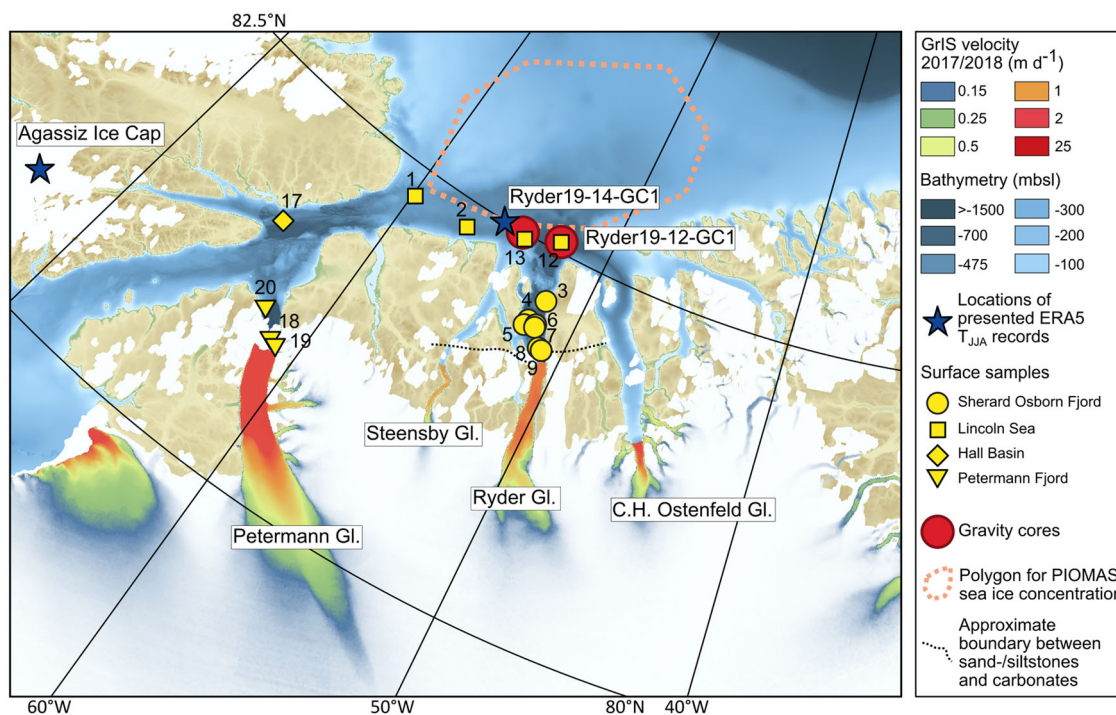


Fig. 4 Southern Lincoln Sea and northern Nares Strait including locations discussed in the manuscript. Surface samples (yellow symbols with area-coded shape) are numbered according to the respective multi-corer station. The locations of gravity core 12-GC and 14-GC are marked with red dots. Additionally the bathymetry (IBCAO v4)⁹⁶ and velocity of the GrIS⁹⁷ are shown and the major glaciers of the region and locations of presented temperature records (blue stars) are marked. The dashed black line marks the approximate boundary of sand-/siltstones and carbonates in the region surrounding Sherard Osborn Fjord⁷⁵.

compilations suggest summer warming of up to 1 °C (compared to PI) between 30–90°N during the Early Holocene⁶⁸, which compares to a (marine and terrestrial) temperature proxy stack for the same latitudinal band (relative to 1961–1990)⁶⁹. Mean annual temperatures from model simulations, on the other hand, are colder than the PI reference until ~9 ka⁶⁸. For central Iceland, Flowers et al.⁷⁰ find a maximum Early Holocene warming of 3.5 °C (compared to 1961–1990). Similar to average MAAT (compared to PI) at Agassiz ice cap for the interval of seasonal sea-ice during the Early Holocene (~11.3 ± 0.6 to 9.7 ± 0.6 cal ka BP), which are 3.6 ± 1.1 °C (Fig. 2). This highlights the complexity of Early Holocene temperature reconstructions in the Northern Hemisphere, which likely arises from proxy biases and regional differences in both the timing and expression of Early Holocene warmth.

Nonetheless, an MAAT of 3.6 ± 1.1 °C at Agassiz ice cap between ~11.3 cal ka BP and 9.7 cal ka BP, falls within the range of projected mean annual Arctic air temperature anomalies (3–5 °C) for a global warming threshold of 2 °C (compared to PI). While these numbers are not directly comparable, as one is representative of the whole Arctic, while the other represents a regional signal over land at an altitude > 1000 m, MAAT during the Early Holocene in the wider Lincoln Sea region were most likely within the range of projected Arctic temperatures for a mean global warming of 2 °C (compared to PI).

Our results thus suggest that we can expect a transition to seasonal sea-ice in the southern Lincoln Sea for a global mean warming of 2 °C compared to the PI. Under high greenhouse gas emission scenarios (SSP2-4.6, SSP3-7.0, and SSP5-8.5), 2 °C warming (compared to PI) will likely be reached by the middle of this century⁷¹. While the Early Holocene record also demonstrates that a sea-ice regime shift in the southern Lincoln Sea is reversible within the reconstructed temperature range, unforeseen feedbacks may occur (e.g., ice arch failure in Nares Strait (Supplementary Discussion 2.1)). This highlights the importance of the 1.5 °C global warming target and the significance of adhering to ‘The Paris Agreement’ for the protection of the unique environments of the Arctic Ocean.

Methods

Site Ryder19-12-GC1 and Ryder19-14-GC1. Sites Ryder19-12-GC1 (82.58°N, –52.53°W, 867 m water depth, 273.5 cm sediment recovery) and Ryder19-14-GC1 (82.51°N, –54.45°W, 580 m water depth, 306.5 cm sediment recovery) are located in the glacially-carved through system that extends northward from Nares Strait and the northern Greenland fjords onto the Lincoln Sea shelf (Fig. 4). 12-GC is located north of Sherard Osborn Fjord, on glacial lineations coming out of Victoria Fjord, suggesting that the site is influenced by the activities of both Ryder Glacier, which drains about 1.6% of the GrIS, and C.H. Ostenfeld Glacier, which drains about 0.6% of the GrIS by area⁷². 14-GC, on the other hand, lies further to the West, north of St Georges Fjord where Steensby Glacier drains about 0.3% of the GrIS⁷³ (Fig. 4). Under present day conditions, both sites are bathed in modified Atlantic Water at the bottom, with a cold and fresh mixed layer (core at 50 m) at the surface⁷⁴.

Lithology. In 12-GC four major lithological units (LU) can be distinguished, while 14-GC only recovered three of the four LU’s defined in 12-GC (Supplementary table 1). 12-GC ends in a glacial diamict (LU4), characterized by unsorted sediment and large clasts (Fig. 5). LU4 thus marks the retreat of grounded ice from the site. Above the diamict, distinctly laminated silty-clay characterizes LU3 (Fig. 5), suggesting sedimentation of glacial melt-water plumes in a proximal to distal glacial marine environment. In the bottom of LU3, laminae are irregular, with layers/lenses of coarser material (LU3b) (Fig. 5), suggesting deposition in a more proximal glacial environment. The same type of laminations is present in the bottom of 14-GC (Fig. 5). The transition from LU3b to LU3a around 202.5 cm in 12-GC and 277 cm in 14-GC, is marked by the onset of pronounced cross-cutting and less coarse laminae (Fig. 5). Reduced input of coarse material is in line with the deglacial retreat of local glaciers into the fjords⁷⁵, while cross-cutting indicates the influence of currents on laminae deposition. This can be either currents related to meltwater discharge at the grounding zone of local glaciers or ocean currents over the Lincoln Sea shelf. Towards the top of LU3a the character of laminations changes to wavy laminae without pronounced cross-cutting in 14-GC and wavy to

planar laminae in 12-GC (Fig. 5), in line with a transition from proximal to more distal glacial marine sedimentation.

Above LU3, both cores record a transitional unit (LU2) of silty clay with a lighter sediment color, high Ca/Ti ratios and increased bulk densities (Fig. 5). While Ca/Ti ratios in 12-GC increase steadily throughout LU3, the increase in 14-GC Ca/Ti is abrupt at the LU3/LU2 boundary (Fig. 5). During the deglacial and early Holocene the delivery of Ca-rich sediments to the fjords and Lincoln Sea shelf was controlled by the retreat of contributing glaciers behind the zone of Silurian sand/siltstones close to the fjord mouths and into the Cambrian/Silurian carbonates of the Franklinian Basin, characterizing the hinterland^{75,76} (Fig. 4). Differences in Ca/Ti in 12-GC1 and 14-GC1 throughout LU3 thus point to (partly) different sediment sources such as Ryder, Steensby, and C.H. Ostenfeld Glacier (Fig. 4). The transitional unit LU2 is a consistent feature in Holocene sediment cores from the area^{75,77,78}. Inside Sherard Osborn Fjord, LU2 corresponds to laminated, meltwater/suspension settling derived Ca-rich sediments, consistent with glacial erosion of the surrounding platform carbonates in the hinterland of Ryder Glacier⁷⁵. In 12-GC and 14-GC, higher bulk densities, slightly coarser material, and more mottled/lenticular sedimentation, indicate a higher energy depositional environment in LU2 compared to LU3. It is unclear, however, if this is related to oceanic currents, or regional glacier dynamics. LU1 can be divided in sub-facies LU1a and LU1b. LU1a is characterized by bioturbated homogenous sediments, while LU1b is characterized by a distinct brown color, accompanied by a drop in both XRF Ca/Ti and bulk densities (Fig. 5). LU1b is especially pronounced in 12-GC (Fig. 5). In the lower part of LU1, both cores show evidence for deposition of ice rafted debris (IRD). In 12-GC, IRD is constrained to the LU2/LU1 boundary, while it is evident from the base of LU1 to ca. 22 cm in 14-GC (Fig. 5).

Chronology. The chronology of 12-GC and 14-GC is based on seven (Supplementary table 2) and five (Supplementary table 3) benthic foraminiferal radiocarbon dates, respectively, and has been developed further from Cronin et al.⁴⁷. Radiocarbon dates were substantiated with two age-depth tie points based on macroscopic observations of lithological transitions and consideration of linear sedimentation rate patterns. Radiocarbon measurements were performed at the National Ocean Sciences Accelerator Mass Spectrometry (NOSAMS) facility at Woods Hole Oceanographic Institution, Massachusetts, USA. Three radiocarbon dates were excluded from the final age model. In 12-GC the radiocarbon date at 94 cm (OS-159561) suggests an age reversal (Supplementary table 2), similar to the radiocarbon date at 49 cm in 14-GC (OS-159564) (Supplementary table 3). Both of these dates are from the transitional unit LU2 (Fig. 6). The distinct change towards lighter colors in LU2 (Fig. 5) might suggest a different sediment source, with the older radiocarbon ages indicating re-deposition of previously deposited sediments. Additionally, the radiocarbon date from the core catcher (CC) of 14-GC (OS-152304) has been excluded, as it is younger than the preceding date at 180 cm (Supplementary table 3). A too young CC age, likely results from the coring process, where younger foraminifera are incorporated into the core catcher when the gravity corer penetrates the sediment.

Radiocarbon ages were calibrated in OxCal v.4.4⁷⁹ using the Marine20 calibration curve⁸⁰. Since the cores are in close proximity, radiocarbon ages were modelled in a combined approach using additional age-depth control points. The top of both cores was assumed to be modern, using a uniform distribution between 0 cal yrs BP and –70 cal years BP, for the age modelling. Additionally, two age-depth tie points were included in the model (Supplementary table 4). One at the top of the Ca/Ti-rich transitional unit and one at the LU3a/b boundary (Fig. 5). For both tie points, the age was extracted from 12-GC due to better radiocarbon age control and used as age control points in the 14-GC age model. Lastly, the top of LU3 at 104 cm and 61 cm in 12-GC and 14-GC respectively, was added as a boundary⁷⁹ to the age model. Throughout LU3, 12-GC and 14-GC have similar sedimentation rates (0.08 cm/yr and 0.1 cm/yr, respectively), suggesting regionally consistent sedimentation patterns. However, while radiocarbon dates in 12-GC indicate a drop in sedimentation rate at the LU3/LU2 transition, in 14-GC this drop occurs already within LU3, possibly due to the lack of radiocarbon age control at the LU3/LU2 transition. Adding a boundary into the age model forces the drop in sedimentation rates to occur at the LU3/LU2 transition, as indicated by radiocarbon dates in 12-GC (Fig. 6).

There is no information on the marine reservoir correction (ΔR) for the Lincoln Sea, with published estimates from the wider northern Greenland region ranging from 0 to 770 years using the Marine09 and Marine13 calibration curves⁷⁵. O’Regan et al.⁷⁵ conclude that given the large uncertainty in published reservoir corrections, a ΔR of 300 ± 300 years is a suitable approximation for Lincoln Sea sites bathed in modified AW. Using Marine20, a ΔR of 300 ± 300 years encompasses previously published reservoir corrections, corresponding to a ΔR of 150–750 years when applying Marine09 or Marine13. Further, applying the same ΔR as O’Regan et al.⁷⁵ allows direct comparison of the new data with previously published results from the Ryder 2019 research cruise.

Modelling the ages of both cores together, including a ΔR of 300 ± 300, allows the modelled ΔR to shift considerably (408 ± 12 (1 σ), $n = 10$), resulting from the large uncertainty in the provided reservoir age. To avoid this shift, which is not based on available knowledge but merely a modelling artifact, three separate age-depth models with a ΔR of 300 ± 0, 0 ± 0, and 600 ± 0 were calculated, where the

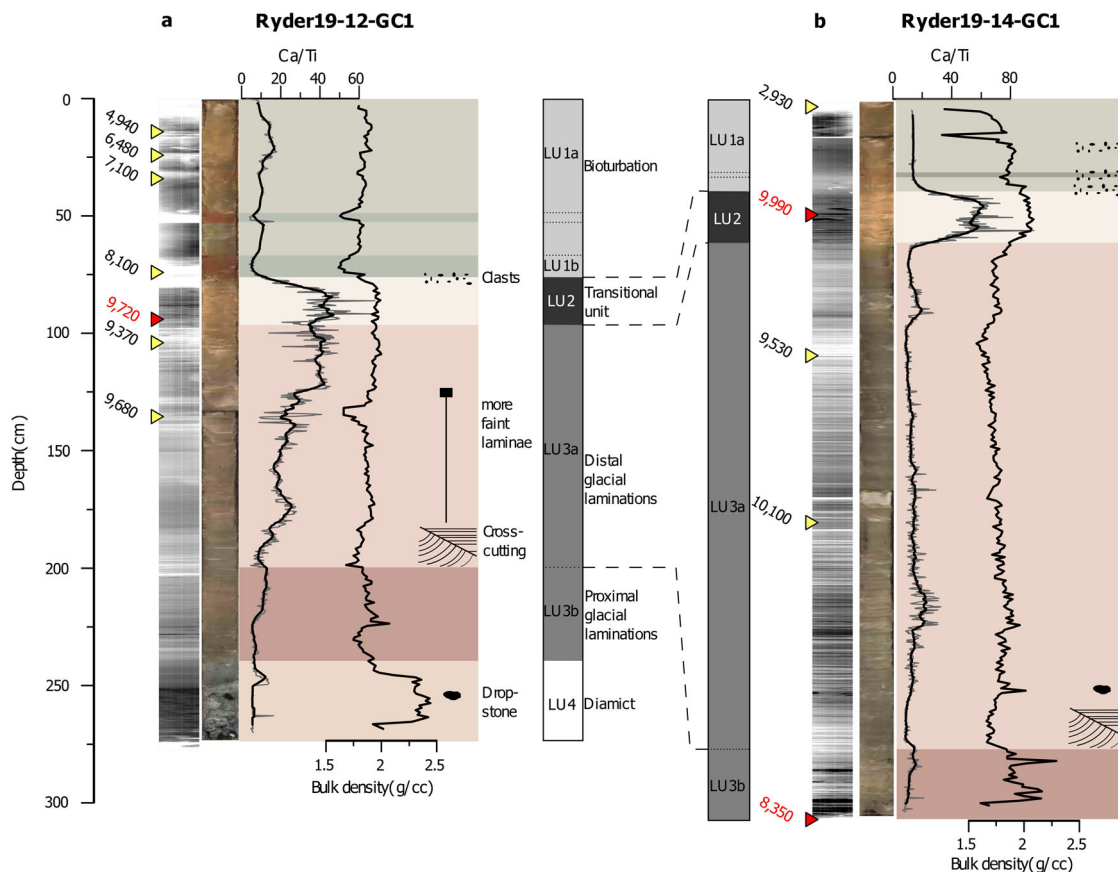


Fig. 5 Lithology of 12-GC and 14-GC. Radiograph, core photo, XRF Ca/Ti (grey, 20-pt average in black) and bulk density (black) of (a) 12-GC and (b) 14-GC, including prominent sedimentary features (dropstones, cross-cutting, IRD/clasts). Key lithological boundaries can be correlated between 12-GC and 14-GC, for the respective depth of LU boundaries see Supplementary table 1. Uncalibrated radiocarbon ages and their respective depth are marked with yellow triangles. Red triangles mark outliers, which are excluded from the final age model.

reservoir correction was subtracted from the ^{14}C age prior to modelling, rather than including a ΔR term in the model. This keeps the reservoir correction fixed and provides an envelope of potential ages, based on the uncertainty in the regional reservoir correction. The final age model suggests that 12-GC covers the time span from the present to ca. 12.7 cal ka BP, while 14-GC reaches back to approximately 11.5 cal ka BP (Fig. 6).

Biomarker extraction and analysis. Sea-ice conditions in the southern Lincoln Sea were reconstructed based on the identification of source-specific highly branched isoprenoid (HBI) and common sterol biomarkers. Mono- and di-unsaturated HBIs, also called IP_{25} (Ice proxy with 25 carbon atoms) and HBI II, respectively, are sympagic biomarkers, produced by sea-ice dwelling diatoms during spring^{41,81}. Their occurrence in sediments is thus used as an indicator of the presence of seasonal sea-ice in the overlying surface ocean. The source of HBI II is less constrained compared to IP_{25} , although studies suggest co-production of IP_{25} and HBI II in the sympagic diatom species *Haslea spicula*, *H. kjellmanii*, and *Pleurosigma stuxbergii* var. *rhomboids*⁸¹. Typically, HBI II and IP_{25} co-vary in Arctic sediments with HBI II occurring in higher concentrations⁴². In addition to sea-ice, salinity might affect the production of IP_{25} ⁸². This is especially important in fjord systems where meltwater discharge might cause large changes in the surface ocean salinity⁸².

Alongside IP_{25} and HBI II, brassicasterol was analyzed. Sterols are common compounds in eukaryotic cell membranes, occurring in both marine and terrestrial organic matter, albeit in different relative concentrations^{83–87}. In the marine realm, brassicasterol is typically derived from phytoplankton sources, including diatoms and dinoflagellates^{84,85,87}.

Biomarkers were extracted from 6 ± 0.1 g freeze dried sediment. A procedural blank and reference sediment sample (~ 3 g) with known biomarker concentrations were added to every extraction batch ($n = 10$). Prior to extraction $0.1 \mu\text{g}$ of 9-Octylheptadec-8-ene (9-OHD) and 5α -androster-16-en-3 α -ol were added to each sample, blank and reference sediment as internal standards for HBIs and sterols, respectively. The samples were extracted three times with dichloromethane/methanol (DCM/MeOH, 2:1 v/v) using sonication (15 min) on the first step and vortexing (1 min) on the second and third step. Following centrifuging the supernatant of each extraction step was transferred to a new sample vial and dried

under a gentle stream of N_2 . The different lipid classes were separated according to polarity using silica column chromatography. Nonpolar lipids, such as IP_{25} and HBI II were eluted with hexane, while the more polar sterols were eluted with DCM:MeOH (1:1, v/v) (~ 7 mL, each). Prior to analysis the sterol fractions were derivatized using *N,O*-bis(trimethylsilyl)trifluoroacetamide (50 μL , 70 $^\circ\text{C}$, 1 h) and diluted with 0.5 mL DCM. HBI fractions were diluted with 50 μL hexane.

All samples were analysed at Aarhus University using an Agilent 7890B gas chromatograph (GC) fitted with an HP-5ms Ultra Inert column (30 m \times 0.25 mm \times 0.25 μm) coupled to a 5977 A series mass selective detector and equipped with a Gerstel multipurpose sampler. For GC-MS operating conditions see Supplementary table 5. The identification of individual lipids is based on the characteristic retention indices and mass spectra of the individual compounds in the reference sediment. In the samples, HBI concentrations were too low to derive a characteristic mass spectrum in GC-MS scan mode. Quantification is achieved by comparing the integrated peak area (PA) of the selected ion for each biomarker (Supplementary table 5) to the PA of the respective internal standard⁸⁸ under consideration of an instrumental response factor (based on the reference sediment) and the mass or the total organic carbon (TOC) concentrations of the extracted sediment⁸⁸ (Supplementary Methods 1.1).

IP_{25} and HBI II are present in the samples in very low concentrations. Thus, for quality control, only samples where both a distinct IP_{25} and HBI II peak could be identified were quantified. In all other samples, the concentrations of both biomarkers were set to zero, in this case meaning below the level of quantification.

IP_{25} and brassicasterol were combined in the P_BIP_{25} index (Eq. 1), a semi-quantitative index of past sea-ice concentration^{89,90}. P_BIP_{25} varies between 0 and 1, with values close to 1 suggesting extensive to perennial sea-ice cover, while values between 0.2 and 0.6 have been suggested to reflect seasonal sea-ice conditions with various seasonal duration of the ice cover⁴².

$$\text{P}_B\text{IP}_{25} = \text{IP}_{25} / (\text{IP}_{25} + (\text{brassicasterol} * c)) \quad (1)$$

$$c = \text{mean IP}_{25} / \text{mean brassicasterol}$$

TOC, TN and $\delta^{13}\text{C}_{\text{org}}$ analyses. For the analysis of TOC, 20–30 mg of freeze-dried, homogenized sediment were folded into Ag cups, which were gently rewetted and

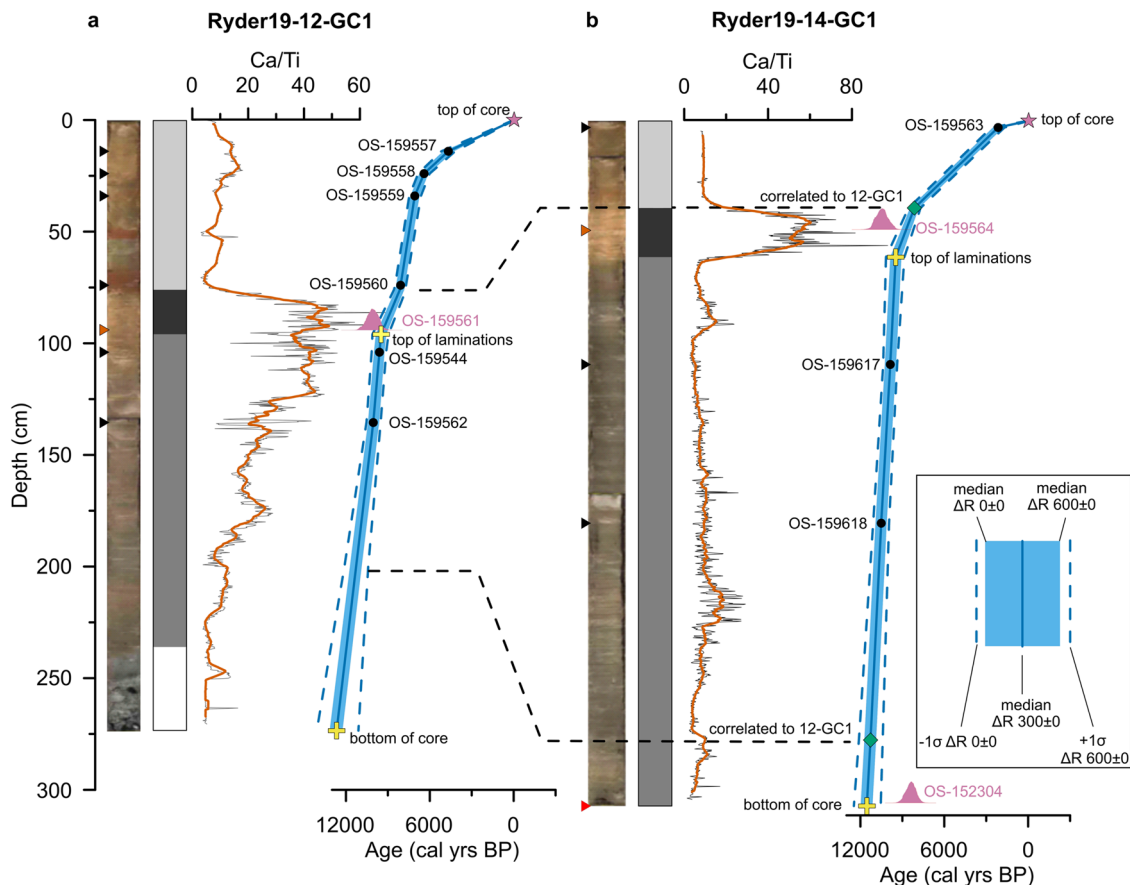


Fig. 6 Age model and correlation of 12-GC and 14-GC. Core photos, schematic of major lithological units (as in Fig. 5), XRF Ca/Ti (black, 20-pt average in red-brown), and age-depth relationship of (a) 12-GC and (b) 14-GC, including the correlation between both cores (horizontal black dashed lines). The depth of individual radiocarbon ages is marked with triangles on the core photos and black dots on the age-depth relationship graph. Boundaries used for age modelling (see text) are marked by yellow crosses, age-depth tie points with green diamonds, and the top of each core is indicated with a pink star. The likelihood distribution (pink) is shown for outlier radiocarbon ages. Both age models include the mean (blue line) based on a ΔR of 300 ± 0 and the uncertainty envelope (light blue) based on a ΔR uncertainty of 300 ($\Delta R = 0 \pm 0$ and $\Delta R = 600 \pm 0$). The dashed blue lines indicated the 1σ uncertainty of the smallest/largest ΔR , respectively.

treated with HCl vapor according to the method outlined in Harris et al.⁹¹. The decalcified sediments were then freeze-dried and analyzed on a Flash 2000 Thermo Scientific elemental analyzer coupled in continuous flow mode to a Thermo Delta V Advantage isotope ratio mass spectrometer at Copenhagen University. Soil standards (Elemental Microanalysis, Okehampton, UK) were used for elemental analyser mass calibration. As working standard for isotope ratio analysis pure gases of ^{13}C -sucrose and ^{13}C -benzoic acid (IAEA, Vienna, Austria) were used.

Reanalysis data. June–August temperature (T_{JJA}) data between 1979 and 2019 are from the ERA5 reanalysis⁶⁴ available from the Copernicus Climate Data Store (<https://cds.climate.copernicus.eu/cdsapp#!/dataset/reanalysis-era5-single-levels-monthly-means?tab=overview>). Data were extracted for the grid points closest to the Agassiz ice cores (80.75 °N, 73 °W, 1740 m MSL) and the core sites of 12-GC and 14-GC (82.5 °N, 55 °W, 0 m MSL). Monthly mean values of June, July and August were averaged for every given year. The shown data (Fig. 3) represent the 2 m air temperature over the land/ocean surface.

Annual mean sea-ice concentration data between 1978 and 2021 are from the Pan-Arctic Ice Ocean Modeling and Assimilation System (PIOMAS) available from the Polar Sciences Center at the University of Washington (http://psc.apl.uw.edu/research/projects/arctic-sea-ice-volume-anomaly/data/model_grid). Data were averaged over the area shown in Fig. 4, with the corner coordinates given in Supplementary table 6. PIOMAS is a coupled ice ocean modeling and assimilation system, combining the Parallel Ocean Program (POP) ocean model with a 12-category thickness and enthalpy distribution (TED) sea-ice model with a viscous-plastic ice rheology⁶⁵. The model grid is a generalized orthogonal curvilinear coordinate system with the northern grid pole located over Greenland (76 °N, 40 °W), giving the highest model resolution in the Greenland Sea, Baffin Bay, and the eastern Canadian Arctic Archipelago⁶⁵. Sea-ice data are validated against buoy, submarine, and satellite observations^{65,92,93}.

Data availability

All biomarker and TOC data shown in this article are available in the Bolin Centre database (<https://bolin.su.se/data/oden-ryder-2019-sediment-detlef-lincoln-sea-1>). ERA5 reanalysis data can be downloaded from the Copernicus Climate Data Store at <https://cds.climate.copernicus.eu/cdsapp#!/dataset/reanalysis-era5-single-levels-monthly-means?tab=overview>. PIOMAS reanalysis data is available from the Polar Sciences Center at the University of Washington (http://psc.apl.uw.edu/research/projects/arctic-sea-ice-volume-anomaly/data/model_grid).

Received: 24 August 2022; Accepted: 17 February 2023;

Published online: 20 March 2023

References

1. Kwok, R. Arctic sea ice thickness, volume, and multiyear ice coverage: Losses and coupled variability (1958–2018). *Environ. Res. Lett.* **13**, 105005 (2018).
2. Lannuzel, D. et al. The future of Arctic sea-ice biogeochemistry and ice-associated ecosystems. *Nat. Clim. Chang.* **10**, 983–992 (2020).
3. Meier, E. N. et al. Arctic sea ice in transformation: A review of recent observed changes and impacts on biology and human activity. *Rev. Geophys.* **52**, 185–217 (2020).
4. Dai, A., Luo, D., Song, M. & Liu, J. Arctic amplification is caused by sea-ice loss under increasing CO_2 . *Nat. Commun.* **10**, 1–13 (2019).
5. Laliberté, F., Howell, S. E. L. & Kushner, P. J. Regional variability of a projected sea ice-free Arctic during the summer months. *Geophys. Res. Lett.* **43**, 256–263 (2016).
6. Notz, D. & SIMP Community. Arctic Sea Ice in CMIP6. *Geophys. Res. Lett.* **47**, e2019GL086749 (2020).

7. Wei, T., Yan, Q., Qi, W., Ding, M. & Wang, C. Projections of Arctic sea ice conditions and shipping routes in the twenty-first century using CMIP6 forcing scenarios. *Environ. Res. Lett.* **15**, 104079 (2020).
8. Sou, T. & Flato, G. Sea Ice in the Canadian Arctic Archipelago: Modeling the Past (1950–2004) and the Future (2041–60). *J. Clim.* **22**, 2181–2198 (2009).
9. Wang, M. & Overland, J. E. A sea ice free summer Arctic within 30 years? *Geophys. Res. Lett.* **36**, L07502 (2009).
10. Holland, M. M., Bitz, C. M. & Tremblay, B. Future abrupt reductions in the summer Arctic sea ice. *Geophys. Res. Lett.* **33**, 23503 (2006).
11. Mahlstein, I. & Knutti, R. September Arctic sea ice predicted to disappear near 2 °C global warming above present. *J. Geophys. Res. Atmos.* **117**, 6104 (2012).
12. Maslanik, J., Stroeve, J., Fowler, C. & Emery, W. Distribution and trends in Arctic sea ice age through spring 2011. *Geophys. Res. Lett.* **38**, L13502 (2011).
13. Moore, G. W. K., Schweiger, A., Zhang, J. & Steele, M. Spatiotemporal variability of Sea Ice in the Arctic's Last Ice area. *Geophys. Res. Lett.* **46**, 11237–11243 (2019).
14. Pfirman, S., Tremblay, B., Fowler, C. & Newton, R. The last arctic sea ice refuge. *Circ.* **4**, 6–8 (2009).
15. Newton, R., Pfirman, S., Tremblay, L. B. & DeRepentigny, P. Defining the “Ice Shed” of the Arctic Ocean's last ice area and its future evolution. *Earth's Futur.* **9**, e2021EF001988 (2021).
16. Heikkilä, M., Ribeiro, S., Weckström, K. & Pienkowski, A. J. Predicting the future of coastal marine ecosystems in the rapidly changing Arctic: The potential of palaeoenvironmental records. *Anthropocene* **37**, 100319 (2022).
17. Schweiger, A. J., Steele, M., Zhang, J., Moore, G. W. K. & Laidre, K. L. Accelerated sea ice loss in the Wandel Sea points to a change in the Arctic's Last Ice Area. *Commun. Earth Environ.* **2**, 1–11 (2021).
18. Moore, G. W. K., Howell, S. E. L. & Brady, M. First Observations of a Transient Polynya in the Last Ice Area North of Ellesmere Island. *Geophys. Res. Lett.* **48**, e2021GL095099 (2021).
19. Moore, G. W. K., Schweiger, A., Zhang, J. & Steele, M. Spatiotemporal Variability of Sea Ice in the Arctic's Last Ice Area. *Geophys. Res. Lett.* **46**, 11237–11243 (2019).
20. Vincent, R. F. A Study of the North Water Polynya Ice Arch using Four Decades of Satellite Data. *Sci. Rep.* **9**, 1–12 (2019).
21. Moore, G. W. K. & McNeil, K. The Early Collapse of the 2017 Lincoln Sea Ice Arch in Response to Anomalous Sea Ice and Wind Forcing. *Geophys. Res. Lett.* **45**, 8343–8351 (2018).
22. Kwok, R., Toudal Pedersen, L., Gudmandsen, P. & Pang, S. S. Large sea ice outflow into the Nares Strait in 2007. *Geophys. Res. Lett.* **37**, L03502 (2010).
23. Goosse, H., Driesschaert, E., Fichefet, T. & Loutre, M. F. Information on the early Holocene climate constrains the summer sea ice projections for the 21st century. *Clim. Past* **3**, 683–692 (2007).
24. Laliberté, F., Howell, S. E. L. & Kushner, P. J. Regional variability of a projected sea ice-free Arctic during the summer months. *Geophys. Res. Lett.* **43**, 256–263 (2016).
25. Berger, A. & Loutre, M. F. Insolation values for the climate of the last 10 million years. *Quat. Sci. Rev.* **10**, 297–317 (1991).
26. Kaufman, D. et al. Holocene global mean surface temperature, a multi-method reconstruction approach. *Sci. Data* **7**, 1–13 (2020).
27. Stranne, C., Jakobsson, M. & Björk, G. Arctic Ocean perennial sea ice breakdown during the Early Holocene Insolation Maximum. *Quat. Sci. Rev.* **92**, 123–132 (2014).
28. Hörner, T., Stein, R., Fahl, K. & Birgel, D. Post-glacial variability of sea ice cover, river run-off and biological production in the western Laptev Sea (Arctic Ocean) – A high-resolution biomarker study. *Quat. Sci. Rev.* **143**, 133–149 (2016).
29. Stein, R. & Fahl, K. A first southern Lomonosov Ridge (Arctic Ocean) 60 ka IP25 sea-ice record. *Polarforschung* **82**, 83–86 (2012).
30. Fahl, K. & Stein, R. Modern seasonal variability and deglacial/Holocene change of central Arctic Ocean sea-ice cover: New insights from biomarker proxy records. *Earth Planet. Sci. Lett.* **351–352**, 123–133 (2012).
31. Wu, J. et al. Deglacial to Holocene variability in surface water characteristics and major floods in the Beaufort Sea. *Commun. Earth Environ.* **1**, 1–12 (2020).
32. Pienkowski, A. J. et al. Seasonal sea ice persisted through the Holocene Thermal Maximum at 80°N. *Commun. Earth Environ.* **2**, 1–10 (2021). 2021 21.
33. Müller, J., Massé, G., Stein, R. & Belt, S. T. Variability of sea-ice conditions in the Fram Strait over the past 30,000 years. *Nat. Geosci.* **2**, 772–776 (2009).
34. Müller, J. et al. Holocene cooling culminates in sea ice oscillations in Fram Strait. *Quat. Sci. Rev.* **47**, 1–14 (2012).
35. Syring, N. et al. Holocene changes in sea-ice cover and polynya formation along the eastern North Greenland shelf: New insights from biomarker records. *Quat. Sci. Rev.* **231**, 106173 (2020).
36. Syring, N. et al. Holocene interactions between glacier retreat, sea ice formation, and Atlantic water advection at the inner Northeast Greenland continental shelf. *Paleoceanogr. Paleoclimatol.* **35**, e2020PA004019 (2020).
37. Hanslik, D. et al. Quaternary Arctic Ocean sea ice variations and radiocarbon reservoir age corrections. *Quat. Sci. Rev.* **29**, 3430–3441 (2010).
38. Cronin, T. M. et al. Quaternary Sea-ice history in the Arctic Ocean based on a new Ostracode sea-ice proxy. *Quat. Sci. Rev.* **29**, 3415–3429 (2010).
39. Funder, S. et al. A 10,000-year record of Arctic Ocean Sea-ice variability - View from the beach. *Science* (80). **333**, 747–750 (2011).
40. England, J. H. et al. A millennial-scale record of Arctic Ocean sea ice variability and the demise of the Ellesmere Island ice shelves. *Geophys. Res. Lett.* **35**, L19502 (2008).
41. Belt, S. T. Source-specific biomarkers as proxies for Arctic and Antarctic sea ice. *Org. Geochem.* **125**, 277–298 (2018).
42. Kolling, H. M. et al. Biomarker Distributions in (Sub)-Arctic Surface Sediments and Their Potential for Sea Ice Reconstructions. *Geochemistry, Geophys. Geosystems* **21**, e2019GC008629 (2020).
43. Randelhoff, A. et al. Pan-Arctic ocean primary production constrained by Turbulent nitrate fluxes. *Front. Mar. Sci.* **7**, 2296–7745 (2020).
44. Detlef, H. et al. Sea ice dynamics across the Mid-Pleistocene transition in the Bering Sea. *Nat. Commun.* **9**, 941 (2018).
45. Belt, S. T. et al. Identification of paleo Arctic winter sea ice limits and the marginal ice zone: Optimised biomarker-based reconstructions of late Quaternary Arctic sea ice. *Earth Planet. Sci. Lett.* **431**, 127–139 (2015).
46. Vincent, W. F. & Mueller, D. Witnessing ice habitat collapse in the Arctic: Abrupt ice loss signals major changes ahead in a north polar conservation zone. *Science* (80). **370**, 1031–1032 (2020).
47. Cronin, T. M. et al. Holocene paleoceanography and glacial history of Lincoln Sea, Ryder Glacier, Northern Greenland, based on foraminifera and ostracodes. *Mar. Micropaleontol.* **175**, 102158 (2022).
48. Seidenkrantz, M.-S. *Cassidulina teretis* Tappan and *Cassidulina neoteretis* new species (Foraminifera): stratigraphic markers for deep sea and outer shelf areas. *J. Micropaleontology* **14**, 145–157 (1995).
49. Wollenburg, J. E. & Mackensen, A. Living benthic foraminifers from the central Arctic Ocean: faunal composition, standing stock and diversity. *Mar. Micropaleontol.* **34**, 153–185 (1998).
50. Cronin, T. M. et al. Late Quaternary paleoceanography of the Eurasian Basin, Arctic Ocean. *Paleoceanography* **10**, 259–281 (1995).
51. Karanovic, I. & Brandão, S. N. The genus *Polycopo* (Polycopidae, Ostracoda) in the North Atlantic and Arctic: Taxonomy, distribution, and ecology. *Syst. Biodivers.* **14**, 198–223 (2016).
52. Gemery, L. et al. An Arctic and Subarctic ostracode database: Biogeographic and paleoceanographic applications. *Hydrobiologia* **786**, 59–95 (2017).
53. Cronin, T. M., Holtz, T. R. & Whatley, R. C. Quaternary paleoceanography of the deep Arctic Ocean based on quantitative analysis of Ostracoda. *Mar. Geol.* **119**, 305–332 (1994).
54. Poirier, R. K., Cronin, T. M., Briggs, W. M. & Lockwood, R. Central Arctic paleoceanography for the last 50 kyr based on ostracode faunal assemblages. *Mar. Micropaleontol.* **88–89**, 65–76 (2012).
55. Hörner, T., Stein, R., Fahl, K. & Birgel, D. Post-glacial variability of sea ice cover, river run-off and biological production in the western Laptev Sea (Arctic Ocean) – A high-resolution biomarker study. *Quat. Sci. Rev.* **143**, 133–149 (2016).
56. De Vernal, A. et al. Natural variability of the Arctic Ocean sea ice during the present interglacial. *Proc. Natl. Acad. Sci. USA* **117**, 26069–26075 (2020).
57. Kaufman, D. et al. Holocene thermal maximum in the western Arctic (0–180°W). *Quat. Sci. Rev.* **23**, 529–560 (2004).
58. Axford, Y., De Vernal, A. & Osterberg, E. C. Past warmth and its impacts during the holocene thermal maximum in Greenland. *Annu. Rev. Earth Planet. Sci.* **49**, 279–307 (2021).
59. Briner, J. P. et al. Holocene climate change in Arctic Canada and Greenland. *Quat. Sci. Rev.* **147**, 340–364 (2016).
60. Cartapanis, O., Jonkers, L., Moffa-Sanchez, P., Jaccard, S. L., & de Vernal, A. Complex spatio-temporal structure of the Holocene Thermal Maximum. *Nat. Commun.* **13**, 1–11 (2022).
61. Lecavalier, B. S. et al. High Arctic Holocene temperature record from the Agassiz ice cap and Greenland ice sheet evolution. *Proc. Natl. Acad. Sci. USA* **114**, 5952–5957 (2017).
62. Dyck, S., Tremblay, L. B., & de Vernal, A. Arctic sea-ice cover from the early Holocene: the role of atmospheric circulation patterns. *Quat. Sci. Rev.* **29**, 3457–3467 (2010).
63. Wu, J. et al. Deglacial to Holocene variability in surface water characteristics and major floods in the Beaufort Sea. *Commun. Earth Environ.* **1**, 1–12 (2020).
64. Hersbach, H. et al. The ERA5 global reanalysis. *Q. J. R. Meteorol. Soc.* **146**, 1999–2049 (2020).
65. Zhang, J. & Rothrock, D. A. Modeling Global Sea Ice with a Thickness and Enthalpy Distribution Model in Generalized Curvilinear Coordinates. *Mon. Weather Rev.* **131**, 845–861 (2003).
66. Casagrande, F., Neto, F. A. B., de Souza, R. B. & Nobre, P. Polar Amplification and Ice Free Conditions under 1.5, 2 and 3 °C of Global Warming as

Simulated by CMIP5 and CMIP6 Models. *Atmosphere (Basel)*. **12**, 1494 (2021).

67. Kaufman, D. S. et al. Holocene thermal maximum in the western Arctic (0–180°W). *Quat. Sci. Rev.* **23**, 529–560 (2004).

68. Zhang, Y., Renssen, H. & Seppä, H. Effects of melting ice sheets and orbital forcing on the early Holocene warming in the extratropical Northern Hemisphere. *Clim. Past* **12**, 1119–1135 (2016).

69. Marcott, S. A., Shakun, J. D., Clark, P. U. & Mix, A. C. A reconstruction of regional and global temperature for the past 11,300 years. *Science* (80). **339**, 1198–1201 (2013).

70. Flowers, G. E. et al. Holocene climate conditions and glacier variation in central Iceland from physical modelling and empirical evidence. *Quat. Sci. Rev.* **27**, 797–813 (2008).

71. Masson-Delmotte, V. et al. *IPCC, 2021: Summary for Policymakers*. (Cambridge University Press). <https://doi.org/10.1017/9781009157896.001>.

72. Rignot, E. & Kanagaratnam, P. Changes in the velocity structure of the Greenland ice sheet. *Science* (80). **311**, 986–990 (2006).

73. Hill, E. A., Carr, J. R. & Stokes, C. R. A review of recent changes in major marine-terminating outlet glaciers in Northern Greenland. *Front. Earth Sci.* **4**, 111 (2017).

74. Jakobsson, M. et al. Ryder Glacier in northwest Greenland is shielded from warm Atlantic water by a bathymetric sill. *Commun. Earth Environ.* **1**, 1–10 (2020).

75. O'Regan, M. et al. The Holocene dynamics of Ryder Glacier and ice tongue in north Greenland. *Cryosphere* **15**, 4073–4097 (2021).

76. Higgins, A. K., Neson, J. R., Peel, J. S., Surlyk, F. & Sønderholm, M. Lower Palaeozoic Franklinian Basin of North Greenland. *Bull. Grønlands Geol. Undersøgelse* **160**, 71–139 (1991).

77. Jennings, A. E. et al. Modern and early Holocene ice shelf sediment facies from Petermann Fjord and northern Nares Strait, northwest Greenland. *Quat. Sci. Rev.* **283**, 107460 (2022).

78. Jennings, A. et al. The holocene history of Nares Strait: Transition from glacial bay to Arctic-Atlantic Throughflow. *Oceanography* **24**, 26–41 (2011).

79. Ramsey, C. B. Bayesian analysis of radiocarbon dates. *Radiocarbon* **51**, 337–360 (2009).

80. Heaton, T. J. et al. Marine20—The Marine Radiocarbon Age Calibration Curve (0–55,000 cal BP). *Radiocarbon* **62**, 779–820 (2020).

81. Brown, T. A., Belt, S. T., Tatarek, A. & Mundy, C. J. Source identification of the Arctic sea ice proxy IP₂₅. *Nat. Commun.* **5**, 4197 (2014).

82. Ribeiro, S. et al. Sea ice and primary production proxies in surface sediments from a High Arctic Greenland fjord: Spatial distribution and implications for palaeoenvironmental studies. *Ambio* **46**, 106–118 (2017).

83. Rontani, J. F. et al. Degradation of sterols and terrigenous organic matter in waters of the Mackenzie Shelf, Canadian Arctic. *Org. Geochem.* **75**, 61–73 (2014).

84. Volkman, J. K. A review of sterol markers for marine and terrigenous organic matter. *Org. Geochem.* **9**, 83–99 (1986).

85. Volkman, J. K. Sterols in microorganisms. *Appl. Microbiol. Biotechnol.* **60**, 495–506 (2003).

86. Yunker, M. B., Macdonald, R. W., Veltkamp, D. J. & Cretney, W. J. Terrestrial and marine biomarkers in a seasonally ice-covered Arctic estuary - integration of multivariate and biomarker approaches. *Mar. Chem.* **49**, 1–50 (1995).

87. Volkman, J. K., Rohjans, D., Rullkötter, J., Scholz-Böttcher, B. M. & Liebezeit, G. Sources and diagenesis of organic matter in tidal flat sediments from the German Wadden Sea. *Cont. Shelf Res.* **20**, 1139–1158 (2000).

88. Belt, S. T. et al. A reproducible method for the extraction, identification and quantification of the Arctic sea ice proxy IP₂₅ from marine sediments. *Anal. Methods* **4**, 705 (2012).

89. Müller, J. et al. Towards quantitative sea ice reconstructions in the northern North Atlantic: A combined biomarker and numerical modelling approach. *Earth Planet. Sci. Lett.* **306**, 137–148 (2011).

90. Smik, L., Cabedo-Sanz, P. & Belt, S. T. Semi-quantitative estimates of paleo Arctic sea ice concentration based on source-specific highly branched isoprenoid alkenes: A further development of the PIP₂₅ index. *Org. Geochem.* **92**, 63–69 (2016).

91. Harris, D., Horváth, W. R. & van Kessel, C. Acid fumigation of soils to remove carbonates prior to total organic carbon or CARBON-13 isotopic analysis. *Soil Sci. Soc. Am. J.* **65**, 1853–1856 (2001).

92. Wang, X. et al. Comparison of Arctic Sea Ice Thickness from Satellites, Aircraft, and PIOMAS Data. *Remote Sens.* **8**, 713 (2016).

93. Schweiger, A. et al. Uncertainty in modeled Arctic sea ice volume. *J. Geophys. Res. Ocean.* **116**, 0–06 (2011).

94. Jansen, E. et al. Past perspectives on the present era of abrupt Arctic climate change. *Nat. Clim. Chang.* **10**, 714–721 (2020).

95. Laskar, J. et al. A long-term numerical solution for the insolation quantities of the Earth. *Astron. Astrophys.* **428**, 261–285 (2004).

96. Jakobsson, M. et al. The International Bathymetric Chart of the Arctic Ocean Version 4.0. *Sci. Data* **7**, 176 (2020).

97. Nagler, T., Rott, H., Hetzenecker, M., Wuite, J. & Potin, P. The Sentinel-1 Mission: New Opportunities for Ice Sheet Observations. *Remote Sens.* **7**, 9371–9389 (2015).

Acknowledgements

Core collection during the *Ryder 2019* expedition was conducted in a responsible manner in accordance with relevant permits and local laws. We would like to thank the captain, crew, and scientific party on the icebreaker *Oden* during the *Ryder 2019* expedition, as well as the Swedish Polar Research Secretariat for supporting the expedition. We are grateful to Carina Johansson (Stockholm University) for sampling of the cores, to Trine Ravn-Jensen (Aarhus University) for laboratory support, and to Per Lennart Ambus (Copenhagen University) for TOC measurements. The *Ryder 2019* expedition was financially supported by the Swedish Polar Research Secretariat, the Centre for Coastal and Ocean Mapping at the University of New Hampshire, Stockholm University, and the Nippon Foundation of Japan. This research has received funding from the Aarhus Universitets Forskningsfond (grant no. AUFF-E-17-7-22 to Christof Pearce), the Vetenskapsrådet (grant no. 2016-04021 and 2021-04512 to Martin Jakobsson; grant no. 2020-04379 to Matt O'Regan, grant no. 2018-04350 to Christian Stranne), the European Union's Horizon 2020 research and innovation programme under the Marie Skłodowska-Curie grant agreement no. 882893 (IceLab), and the European Union's Horizon 2020 research and innovation programme under grant agreement no. 869383 (ECOTIP). Thomas M. Cronin was funded by the U.S. Geological Survey Climate R & D Program. Any use of trade, firm, or product names is for descriptive purposes only and does not imply endorsement by the U.S. Government."

Author contributions

H.D.: Conceptualization, investigation, visualization, funding acquisition, writing (original draft and review & editing). M.O.R.: Conceptualization, funding acquisition, writing (review & editing). C.S.: Investigation, funding acquisition, writing (review & editing). M.M.J.: Investigation, writing (review & editing). M.G.: Funding acquisition, writing (review & editing). T.M.C.: Funding acquisition, writing (review & editing). M.J.: Conceptualization, funding acquisition, writing (review & editing). C.P.: Conceptualization, visualization, funding acquisition, writing (original draft and review & editing).

Competing interests

The authors declare no competing interests.

Additional information

Supplementary information The online version contains supplementary material available at <https://doi.org/10.1038/s43247-023-00720-w>.

Correspondence and requests for materials should be addressed to Henrieka Detlef or Christof Pearce.

Peer review information *Communications Earth & Environment* thanks G.W.K. Moore and the other, anonymous, reviewer(s) for their contribution to the peer review of this work. Primary Handling Editors: Ilka Peeken and Joe Aslin. Peer reviewer reports are available.

Reprints and permission information is available at <http://www.nature.com/reprints>

Publisher's note Springer Nature remains neutral with regard to jurisdictional claims in published maps and institutional affiliations.



Open Access This article is licensed under a Creative Commons Attribution 4.0 International License, which permits use, sharing, adaptation, distribution and reproduction in any medium or format, as long as you give appropriate credit to the original author(s) and the source, provide a link to the Creative Commons license, and indicate if changes were made. The images or other third party material in this article are included in the article's Creative Commons license, unless indicated otherwise in a credit line to the material. If material is not included in the article's Creative Commons license and your intended use is not permitted by statutory regulation or exceeds the permitted use, you will need to obtain permission directly from the copyright holder. To view a copy of this license, visit <http://creativecommons.org/licenses/by/4.0/>.

© The Author(s) 2023